An ER–Horse Detonating Stress Cascade for Hepatocellular Carcinoma Nanotherapy

Xintong Bian
Chongqing Medical University
Ningke Fan
Key Laboratory of Clinical Laboratory Diagnostics (Ministry of Education), College of Laboratory Medicine, Chongqing Medical University
Meng Li
The Second Affliated Hospital of Chongqing Medical University
Daobin Han
Key Laboratory of Clinical Laboratory Diagnostics (Ministry of Education), College of Laboratory Medicine, Chongqing Medical University
Jia Li
The First Affiliated Hospital of Chongqing Medical University
Lu Fan
Key Laboratory of Clinical Laboratory Diagnostics (Ministry of Education), College of Laboratory Medicine, Chongqing Medical University
Xinyu Li
Key Laboratory of Clinical Laboratory Diagnostics (Ministry of Education), College of Laboratory Medicine, Chongqing Medical University
Liangsheng Kong
Key Laboratory of Clinical Laboratory Diagnostics (Ministry of Education), College of Laboratory Medicine, Chongqing Medical University
Hua Tang
Chongqing Medical University
Shijia Ding
Chongqing Medical University
fzngzhou song
Chongqing Medical University
Siqiao Li
Department of Forensic Medicine, Faculty of Basic Medical Sciences, Chongqing Medical University
Wei Cheng (chengwei@hospital.cqmu.edu.cn)
The First Affiliated Hospital of Chongqing Medical University https://orcid.org/0000-0002-1921-9761

Article

Keywords: Endoplasmic reticulum vesicles, homologous recognition, stress cascade, Ca2+ homeostasis disruption, endoplasmic reticulum stress, oxidative stress

Posted Date: October 18th, 2022

DOI: https://doi.org/10.21203/rs.3.rs-2168182/v1

Abstract

Persisting and excessive endoplasmic reticulum stress (ERS) can evoke rapid cell apoptosis. Therapeutic interference of ERS signaling holds enormous potentials for cancer nanotherapy. Herein, a hepatocellular carcinoma (HCC) cell–derived ER vesicle (ERV) encapsulating siGRP94, denoted as ER–horse, has been developed for precise HCC nanotherapy. Briefly, ER–horse, like Trojan horse, was recognized via homotypic camouflage, imitated physiological function of ER and exogenously opened the Ca^{2+} channel. Consequently, the mandatory pouring–in of extracellular Ca^{2+} triggered the aggravated stress cascade (ERS and oxidative stress) and apoptosis pathway with the inhibition of unfolded protein response by siGRP94. Collectively, our findings provide a paradigm for potent HCC nanotherapy via ERS signaling interference and exploring therapeutic interference of physiological signal transduction pathways for precision cancer therapy.

Introduction

Endoplasmic reticulum (ER) is an essential cellular compartment for protein synthesis and maturation.[1–4] The ER stress (ERS) signaling caused by accumulation of unfolded or misfolded proteins inside the ER, is involved in the pathogenesis of various human diseases.[5,6] In human tumors, ERS has been shown to be hyperactivated and beneficial for cancer cell survival in harsh environments.[7] Persistent ERS occurred in tumor cells is manifested as ER homeostasis imbalance, which ultimately impacts cell function, fate and survival.[8–10] Typically, ER homeostasis is restored by unfolded protein response (UPR), eventually adapting to stress and survival. However, persistent or severe ERS can directly lead to cancer cell death.[11] Therefore, therapeutic interference of ERS signaling in the cancer cell will be a potential therapeutic modality. To this end, a variety of anticancer agents towards ERS have been explored, which mainly target UPR components or proteasomes, and have shown promise in clinical trials.[10, 12] Despite these advances, these agents are more suitable for some polysecretory cell types due to the over–dependence on the progress of misfolded protein accumulation.[13–15] It is worth hypothesizing the combination of the early disruption of ER homeostasis and the interference of protein–folding process will realize more effective cancer therapy. Besides, the undesired side effect of the current agents with poor tumor specific distribution also needs to be resolved.[16] Therefore, exogenous nanomedicine intervention for the purpose of activating the body's cell stress system against cancer has gained significant attention and been sought to join traditional treatment modalities as an adjuvant treatment.

One of the approaches disrupting the ER homeostasis is adjusting the Ca^{2+} homeostasis. Under physiological conditions, the ER regulates intracellular Ca^{2+} homeostasis through an endogenous route.[17] When intracellular Ca^{2+} stores become depleted, STIM1, which senses the ER luminal Ca^{2+} concentration, translocates to vesicular structures (punctae) underneath the plasma membrane (PM). Then, STIM1 interacts with ORAI1 and activates calcium release–activated calcium (CRAC) channels residing in the PM, which enables Ca^{2+} entry into the cytoplasm.[18–20] Intracellular Ca^{2+} homeostasis is closely related to the maintenance of normal cell functions,[21, 22] while disruptions in this homeostasis decrease protein

folding capacity, leading to the accumulation of unfolded proteins and eventually ERS, which usually be relieved by UPR.[23–25] However, if UPR does not work effectively, a specific apoptotic cascade pathway of caspase–12 is activated in damaged cells, accompanied by the trigger of oxidative stress (OS).[23, 26–27] Inspired by this, an exogenous biovesicle nanosystem featuring particular physiological changes induced by simulation of ER function is desirable to realize precise cancer therapy and mitigate cytotoxicity.

Mannose–rich ER vesicles (ERVs), which retain the specific properties of the parental tumor cells, can specifically target homologous tumors and derivatives for selective binding.[28–33] In particular, ERVs are considered to manipulate the fate of cells under ERS by activating CRAC channels. Inspired by these natural properties, herein, we report a hepatocellular carcinoma (HCC) cell–targeted ERV encapsulating siGRP94, denoted as ER–horse for the precise nanotheraoy. The ER–horse imitates the physiological regulation function of ER to exert induce cell pathological changes via physiological signal transduction pathways (Fig. 1a). For a proof–of–concept demonstration, HCC cells were selected as the homologous target cells due to high expression of mannose receptor (MR). Usually, HCC cells survive from ERS that caused by Ca^{2+} influx or other adverse microenvironments through the activation of UPR, which is an adaptive mechanism capable of reinstating ER homeostasis (Fig. 1b, top). For the precision treatment, ER–horse sourced from HepG2 cells are developed into a smart platform with the homotypic camouflage recognition ability for permitting entry of the vesicle into source cells, like Trojan horse (Fig. 1b, below). After mannose–MR recognition, STIM1 on ERVs couples with ORAI1 on HepG2 cells to activate CRAC channels. Then, the designed ER–horse triggers stress cascade, starting by the pouring–in of the Ca^{2+}: 1) Ca^{2+} homeostasis disruption, attributing to Ca^{2+} influx from CRAC channels and causing unfolded protein accumulation; 2) ERS, following unfolded protein accumulation and strengthened by siGRP94 release in the cytoplasm; 3) OS, induced by the excessive ERS and aggravating ERS in turn accompanied by the production of reactive oxygen species (ROS);[34] 4) sustained Ca^{2+} homeostasis disruption, deriving from the depletion of ER Ca^{2+} stores and STIM1 protein oligomerization induced by OS, and restarting the circle. This could form a viciously stress cascade, where Ca^{2+} homeostasis disruption, ERS and OS amplify mutually, forcing cells to apoptosis and achieving nanotherapy for HCC (Fig. 1b, below). Therefore, determination of ER–horse with the homotypic recognition–driven targetability and the mechanism triggering the stress cascade is expected to facilitate further tumor therapy development and diverse biomedical applications.

Results

Synthesis and characterization. The ER–horse was prepared with the following three steps (Fig. 1a): 1) ER membrane was isolated from HCC cells (HepG2 cells was used here), 2) ERVs were constructed by extraction and extrusion, and 3) siGRP94 selected as intracellular GRP94 downregulator was encapsulated by extrusion. For control ERVs, only steps 1 and 2 were performed. The mannose expression on ER membrane was verified, which was necessary for the targetability of ER–horse to MR–rich hepatoma cells, by detecting the co–localization of Con A (binding to mannose) and calnexin (CNX)

(an ER chaperone) in the HepG2 cells (Supplementary Fig. 1). The overlapped signals suggested that the ER membranes of HepG2 cells had potential for endowing ER–horse with a mannose–rich character.

The composition and physical properties of the ERVs and ER–horse were investigated. First, the primary protein components of the ER membrane, including CNX, calreticulin (CRT) and the putative calcium sensor STIM1, were detected in ERVs by Western Blotting (WB) (Fig. 2a). Moreover, the ERVs were found to retain surface mannose by fluorescence microscopy, which was important for tumor targeting (Fig. 2a, box in upper right). To ascertain the stability of the ERVs in a physiological environment, we performed dynamic light scattering (DLS) and measured the zeta potential of ERVs incubated in PBS at different pH values (5.5, 6.0 and 7.4). The size (Fig. 2b) and zeta potential (Fig. 2c) of the ERVs changed slightly but not significantly in response to pH, indicating that these vesicles are stable in acidic environments such as the tumor microenvironment.

Then, we explored the specific characteristics of ER–horse and ERVs in PBS at physiological pH (7.4). Transmission electron microscopy (TEM) images showed that the ER–horse exhibited a typical globular morphology (Fig. 2d). Nanoparticle tracking analysis (NTA) showed that the average hydrodynamic diameter of the ER–horse was 187 ± 2.8 nm at a concentration of 2.22e + 09 ± 1.56e + 08 particles/mL (Fig. 2e). Moreover, DLS analyses of ER–horse and ERVs performed at pH 7.4 showed that the two vesicle types maintained nearly the same particle size range centered at approximately 200 nm in a physiological environment (Fig. 2f), consistent with the TEM results, indicating that siGRP94 encapsulation had no impact on vesicle stability. Compared with larger nanoparticles, nanoparticles smaller than 200 nm were more inclined to penetrate tumor tissue due to the enhanced permeability and retention (EPR) effect.[35] To verify the successful encapsulation of siGRP94 in ER–horse, we next compared the zeta potentials of ER–horse, empty ERVs, and siGRP94. The zeta potential of ER–horse was − 7.39 ± 1.28 mV, which was significantly lower than that of siGRP94 (–3.19 ± 0.88 mV) and ERVs (–3.95 ± 1.22 mV) (Fig. 2g). The lower zeta potential of ER–horse reflected the successful encapsulation of siGRP94 by negatively charged ERVs. Prior to biological evaluation of the ER–horse, it was necessary to confirm the integrated structure of it. This desired structure of ER–horse was confirmed by confocal laser scanning microscopy (CLSM) imaging of the ER membrane (red) and siGRP94 (green) (Fig. 2h). The high fluorescence co–localization rate indicated the successful preparation and integrity of ER–horse.

To further examine the biocompatibility of the ER–horse, serum stability assays were performed in which ER–horse or siGRP94 was incubated with 10% fetal bovine serum (FBS). CLSM imaging showed that ERVs protected siGRP94 from nucleases, as evidenced by the continued detection of fluorescence from ER–horse (green) but not from siGRP94 in tumor cells (Supplementary Fig. 2). These results suggested that ER–horse was successfully prepared, and used as a safe and stable delivery system with high practicality for in vivo application.

Homologous cells–targeting ability of ER–horse in vitro. We hypothesized that the ER–horse constructed from the mannose–rich ER membrane would homologously bind to MR–rich HepG2 cells and then activate CRAC channels (Fig. 3a). As the first step in determining the potential mechanisms responsible

for ER–horse–mediated tumor targeting, it was necessary to determine the capacity of ER–horse for targeted recognition of human cell lines, including two liver cancer cell lines (HepG2 and SMMC–7721 cells, hereinafter referred to as 7721 cells), a normal human liver cell line (L02), a normal human breast epithelial cell line (MCF 10A) and a breast cancer cell line (SK–BR–3). Thus, surface MR expression (red) on these cell lines was evaluated by CLSM analysis (Fig. 3b, d). Liver cancer cells (HepG2 and 7721 cells) showed a robust MR fluorescence signal at the cell membrane, with a particularly stronger signal in HepG2 cells than in 7721 cells. The other cell lines showed negligible MR expression, supporting the feasibility of using mannose as the identification element of liver cancer.

To confirm the specific interaction of mannose on ER–horse and MR on HepG2 cells, the co–localization of mannose (green) and MR (red) was investigated after incubating HepG2 cells with ER–horse. The ER–horse treatment group had a higher fluorescence co–localization rate (89.57 ± 3.51%) than the control (untreated) group (18.48 ± 1.61%), indicating the successful targeting of HepG2 cells by ER–horse (Fig. 3c). Subsequently, to verify the requirement for mannose on ER–horse, we blocked the mannose–binding sites on HepG2 cells with free mannose (red) for 1 h. CLSM analysis revealed a lack of cancer cell targeting by ER–horse in the group pretreated with free mannose, demonstrating that the homologous targetability depended on the interaction of mannose on ER–horse and MR on HepG2 cells (Fig. 3e, f).

Next, to verify the ability of ER membrane encapsulation to improve the cellular uptake of ER–horse (green), specific cell lines that differ in their expression of MR (HepG2, 7721, and L02 cells) were investigated at diverse duration (0, 2, 5, 10, and 30 min) (Fig. 3g). CLSM images showed that cells with high MR expression had a strong ability to capture ER–horse. HepG2 cells exhibited strong fluorescence of ER–horse after 10 min of incubation, indicating the time necessary for considerable fusion to occur (Fig. 3g, Supplementary Fig. 3a). At 30 min, the intracellular ER–horse fluorescence intensity was higher in HepG2 cells than in 7721 and L02 cells. The results indicated that the ER–horse was able to specifically identify HepG2 cells rich in MR, which provided the appropriate conditions for subsequent activation of CRAC channels and precise delivery of siGRP94.

To verify that the ability to specifically recognize MR–rich cells was derived from the encapsulation of the ER membrane, we detected the cellular uptake efficiency of vesicles composed of different biomembranes, including ERVs, RBCVs and CCVs (green). Compared to siGRP94–RBCVs and siGRP94–CCVs with a low cellular uptake efficiency, the ER–horse showed markedly greater intracellular fluorescence intensity in a very short time (10 min) (Fig. 3h, Supplementary Fig. 3b). These results indicated that encapsulation by mannose–rich ER membranes could enhance the cellular uptake of ER–horse by HepG2 cells with greater selectivity and specificity.

Furthermore, we observed the coupling of exogenous STIM1 on ER–horse with ORAI1 on the HepG2 cells at the moment of ERV fusion with HepG2 cells (Fig. 3i). The higher fluorescence co–localization rate in the ER–horse–treated group (84.48 ± 3.16%) than the control group (21.8 ± 2.41%) indicated an increase in the binding of STIM1 to ORAI1; moreover, the images showed an increase in STIM1 at the PM upon

exposure of HepG2 cells to ER–horse. Taken together, these results indicated that the ER–horse showed precise homologous targetability to HepG2 cells and assembled CRAC channels (STIM1–ORAI1), which might improve the treatment effect.

Intracellular trafficking mechanisms. After binding to the cell membrane, cellular uptake of ER–horse is the next important step in biovesicle delivery. Therefore, we explored the processes of ER–horse fusion with the PM, endosomal escape and siGRP94 release by monitoring the endocytosis and intracellular distribution of ER–horse (ERVs, red; and siGRP94, green) in HepG2 cells (Fig. 4a). To investigate the fusion of ER–horse with the cell membrane, we labeled the HepG2 cell membrane (green) and monitored the fusion process by CLSM. After 10 min of incubation, the fluorescence signal of ER–horse appeared on the HepG2 cell surface (Fig. 4b), indicating fusion between ER–horse and the cell membrane. At 15–20 min, the ER–horse signal gradually increased before gradually moving away from the cell membrane. As the next step necessary for siGRP94 delivery, the co–localization of ER–horse (green) and endosomes (purple) was assessed to verify the transport of ER–horse into the cytoplasm and the fusion of ER–horse with endosomes. CLSM images showed an increase in fusion between ER–horse and endosomes after incubation for 60 min (Fig. 4c). These results demonstrated that ER–horse was taken up into cells through endocytosis as the form of endosome (Endo)–ERVs.

The endosomal release of siGRP94 near the ER is crucial for overall siRNA–mediated silencing efficiency. Successful delivery of siGRP94 from Endo–ERVs to the ER (red) was evidenced by the separation of the siGRP94 signal (green) from the Endo–ERV signal (purple) (Fig. 4d). During the 30–60 min incubation period, the co–localization (white) of siGRP94 (green), Endo–ERVs (purple) and ER (red) increased, indicating an increase in the delivery of siGRP94 to the ER membrane area by Endo–ERVs. After 90 min of incubation, no co–localization was observed, suggesting that all siGRP94 had been released from the endosomes and delivered to the ER. The targeted release of siGRP94 encapsulated by Endo–ERVs implies that ERVs in Endo–ERVs probably plays an important role in promoting the ER uptake of ER–horse due to the similar features; thus, the homology between Endo–ERVs and the ER membrane immediates membrane fusion. Therefore, the ER–horse is a potential strategy for effectively improving cellular uptake and drug release.

To explore the exact course of endosomal reorganization and escape of siGRP94 molecules in the cytoplasm, the specific dynamic process was characterized in further detail by fluorescence imaging of HepG2 cells. In this experiment, fluorescent–labeled dextran (purple), a water–soluble and membrane–impermeable molecule, was added to the culture medium to label endosomes. As dextran enters the cytosol only if the endosomal membrane is damaged, dextran can be used to assess the integrity of the endosomal membrane during intracellular tracing. CLSM images showed the time–dependent appearance of endosomes (purple), siGRP94 (green) and ERVs (red) in both merged and individual channels (Fig. 4e). After 60 min of incubation, Endo–ERVs containing siGRP94 were visible. Over the next 30 min of monitoring, the fluorescent signal of siGRP94 (green) quickly disappeared, and the fluorescence signals for dextran (purple) and ERVs (red) remained visible and co–localized. These results indicated the rapid escape and complete release of siGRP94 in the constructed system without

endosomal membrane rupture, reasonably indicating a highly efficient membrane fusion mechanism by taking advantage of the transporting process.

Furthermore, we monitored the trafficking of labeled ER–horse (green) from the cell membrane to other intracellular organelles (red) by CLSM for 0–8 h (Supplementary Fig. 4). The fluorescent signal of ER–horse was exclusively observed at the cell membrane (green) at the initial time point (1 h), with a high Pearson's correlation coefficient (~ 0.84). However, after 1 h, the fluorescence intensity of ER–horse at the cell membrane declined, and then the signal appeared at the ER membrane (CNX antibody), indicating that the ER–horse effectively transported siGRP94 to the ER area. Given that the main pathway of membrane transport from the cell membrane to the ER membrane is dependent on endosomal vesicles, these observations provide further evidence for the transport of ER–horse through the endosomal vesicular transport system. After siGRP94 delivered to the ER, fluorescence was observed at the mitochondria (MitoTracker) and lysosomes (LysoTracker) at 4–8 h, indicating the subsequent movement of the ERVs. These results showed the fate of siGRP94 and ERVs in the constructed ER–horse after cellular uptake by HepG2 cells.

Stress cascade induced by ER–horse. Inspired by the effective cellular uptake and delivery of ER–horse, we next verified the specific ability of ER–horse inducing the stress cascade (Fig. 5a). As the indicators of OS, we compared the concentration of ROS in the treatment groups of ERVs and ER–horse (Fig. 5b–d). It is clear that the fluorescence of ROS in ER–horse group is higher than that of ERVs after 12 h treatment. Then, we detected the specific mechanism of cell stresses. Briefly, after treatment with ER–horse, Ca^{2+} influx disrupted Ca^{2+} homeostasis and triggered unfolded protein accumulation, followed by ERS and OS. With the downregulation of ERS protective protein GRP94, UPR was inhibited, while ERS and OS were amplificated and further boosted Ca^{2+} influx to from a vicious cycle, eventually inducing cell apoptosis. While in the ERV group without siGRP94, UPR alleviated the ERS and OS by reducing the accumulation of unfolded protein, and made cells survival. Considering Ca^{2+} influx and ROS production played vital roles in the cyclical process; therefore, we performed CLSM and flow cytometry to determine whether ER–horse enhanced cytoplasmic Ca^{2+} and ROS contents in HepG2 cells (Fig. 5b–d). CLSM images of Ca^{2+} and ROS after treatment with ERVs (Fig. 5b, 5d, below) and ER–horse (Fig. 5c, 5d, below) for different durations (0, 0.5, 1, 4, 8, and 12 h) showed similar increasing trends at 0–1 h (Supplementary Fig. 5a). Increases in the fluorescence signals of Ca^{2+} and ROS over the next 11 h were observed in the ER–horse group, whereas these signals decreased in the ERV group after 4 h. We hypothesized that the interaction of STIM1 and ORAI1 caused by the fusion of ER–horse with the HepG2 cell membrane activated the CRAC channels in the early treatment period, inducing an increase in intracellular Ca^{2+}; and the changes in ROS fluorescence might be the result of ERS sourced by Ca^{2+} homeostasis imbalance in 0–4 h. Then, the fluorescence intensities of Ca^{2+} and ROS continued to increase in the ER–horse group in 4–12 h, indicating that gene silencing by siGRP94 further aggravated ERS. In contrast, the fluorescence signals of Ca^{2+} and ROS in the ERV group tended to recover due to cell self–recovery. Moreover, the fluorescent changes in the different treatment groups (PBS, siGRP94, ERVs, negative control (NC–) ERVs, and ER–

horse) at 1 h verified our hypothesis, that is, the fusion of ERVs to cell membrane could trigger Ca^{2+} influx and increase ROS levels and become parts of stress cascade (Fig. 5d–e, Supplementary Fig. 5b).

To clarify the underlying mechanism by which Ca^{2+} influx is induced by ER–horse in the stress cascade, we monitored intracellular Ca^{2+} mobilization and ROS production in the ER–horse group after cotreatment with different drugs (2–APB, BAPTA and DIDS). The STIM1–ORAI1 calcium channel inhibitor 2–APB and the calcium chelator BAPTA reduced the Ca^{2+} influx induced by ER–horse. A similar effect was not observed following treatment with DIDS, which inhibited the voltage–dependent anion channel type 1 calcium channel on the outer mitochondrial membrane (Fig. 5f, Supplementary Fig. 5c). These data indicated that the increase in cytoplasmic Ca^{2+} originated from both extracellular Ca^{2+} influx and intracellular Ca^{2+} release from the ER in response to the activation of CRAC channels rather than other calcium channels. As for ROS production, cytosolic ROS levels decreased significantly after 2–APB and BAPTA treatment but showed no obvious change after DIDS treatment compared with the control. The trend changes of ROS were roughly consistent with that of Ca^{2+}. Moreover, both BAPTA and 2–APB significantly decreased mitochondrial ROS production induced by ER–horse treatment, indicating that elevated cytoplasmic Ca^{2+} contributed to the increase in ROS, which was consistent with the flow cytometry results (Supplementary Fig. 6).

To further assess the specific targetability of ER–horse to HepG2 cells, we detected the fluorescent signals of cytoplasmic Ca^{2+} and ROS in HepG2 cells treated with different siGRP94–vesicles for 1 h and different cells treated with ER–horse for 0, 1 and 12 h. HepG2 cells treated with ER–horse exhibited higher fluorescence intensities of Ca^{2+} and ROS than those treated with other vesicles or other treated cell types (Supplementary Fig. 7–9). The above results showed that ER–horse could lead to the Ca^{2+} influx and the ROS production via activation of CRAC channels (STIM1–ORAI1).

Since the ERS can be induced by the influx of Ca^{2+} and strongthen by siGRP94, we assessed whether different treatments induced ERS. Ultrastructural changes in the ER in HepG2 cells were observed after different treatments (ER–horse, siGRP94, ERVs). Compared with the siGRP94 and ERV control groups, the ER–horse group showed obvious ER swelling and vacuolization after 36 h of treatment, indicating the occurrence of ERS (Fig. 5g).

Next, the expression levels of ERS–related proteins were assessed by WB. First, the concentration of ER–horse between 0 and 10 μM was optimized for 36 h of incubation (Fig. 5h, top left), and 10 μM ER–horse was chosen for the following experiments. The levels of the classic ERS markers GRP78 were higher in the ERV and ER–horse groups than in the PBS and siGRP94 groups, with a greater increase in the ER–horse group than in the ERV group (Fig. 5h, bottom left). Among the four groups, the ER–horse group had the lowest GRP94 levels due to siRNA–mediated silencing; notably, the GRP94 levels did not decrease in the ERV group. Given the induction of ERS, we next determined the levels of the apoptosis–related protein Bcl–2 and the apoptosis regulator BAX to confirm the involvement of apoptosis. The expression of Bcl–2 levels were lower while no significant change in Bax in HepG2 cells treated with ER–horse group

compared with those of PBS, siGRP94, or ERVs group. To verify the effect of siGRP94 in inhibiting the UPR, we determined GRP94 and GRP78 protein expressions in the two groups (the ERV and ER–horse groups) of HepG2 cells for different times (0, 2, 4, 8, and 12 h) (Fig. 5h, right). Treatment with ER–horse evoked a continued increase in GRP94 protein from 0–4 h due to ERS caused by subsequent Ca^{2+} influx and ROS production. At 8–12 h, siGRP94–mediated silencing induced decreases in GRP94 levels, which further aggravated ERS. Simultaneously, the corresponding levels of the ERS–related protein GRP78 increased in a time–dependent manner throughout the time course. Conversely, in the ERV group, GRP94 levels peaked at 8 h and then declined, which was consistent with the change in GRP78 (Fig. 5h, bottom right). This difference was hypothesized to stem from the absence of siRNA–mediated silencing, which might allow the activation of cell self–regulation and recovery.

Therapeutic effect in vitro. To further explore the apoptotic pathway induced by ER–horse, a series of apoptosis–related proteins (caspase–12, CHOP, TRAF2, Cl–caspase–3) expressions were investigated. WB analysis demonstrated the high expression of cascade pathway of caspase–12 related proteins, indicating cells apoptosis through a specific apoptotic cascade pathway of caspase–12. (Fig. 6a). ER–horse can augment nanotherapy efficiency by triggering ERS aggravation and GRP94 downregulation to disrupt the self–repair function of cancer cells. To corroborate the antitumor potential, the induction of apoptosis in response to ER–horse treatment was assessed by CLSM. HepG2, 7721 and L02 cells were treated for 36 h with ER–horse, and propidium iodide (PI) staining was used to identify apoptotic cells. Compared with 7721, L02 and HepG2 control cells (no ER–horse treatment), HepG2 cells treated with ER–horse showed higher fluorescence signals, indicating that ER–horse induced the apoptosis of HepG2 cells (Fig. 6b). Additionally, Cell Counting Kit–8 (CCK–8) experiments were performed from 0 to 36 h to compare the survival rates of HepG2 cells subjected to different treatments (PBS, siGRP94, ERVs, and ER–horse) (Fig. 6c), HepG2 cells treated with different vesicles (ER–horse, siGRP94–RBCVs, and siGRP94–CCVs) (Fig. 6d) and different cells (HepG2, 7721, and L02 cells) treated with ER–horse (Fig. 6e). The survival rates of HepG2 cells with different treatment groups illustrated that the cell apoptosis induction by ER–horse was the best among other control groups (with survival rates of 45.66% for ER–horse group, 83.76% for ERVs group and 92.2% for siGRP94 group). In addition, compared with siGRP94–RBCVs and siGRP94–CCVs, ER–horse clearly had the greatest antitumor effects (with survival rates of 46.6% for ER–horse group, 74.77% for siGRP94–RBCVs group, and 83.49% for siGRP94–CCVs group) on HepG2 cells due to their tumor–targeting ability and the presence of STIM1 on the surface. Obviously, the antitumor effects of ER–horse on HepG2 cells were superior to those on the other two cell types due to their different uptake efficiencies of ER–horse (with survival rates of 44.17% for HepG2 cells, 70.63% for 7721cells, and 84.99% for L02 cells). The results suggested that ER–horse decreased HepG2 cell viability and induced cell apoptosis in a time–dependent manner. Furthermore, to verify the effect of the activation of CRAC on the antitumor effect, we assessed HepG2 cell survival after pretreatment with 2–APB, BAPTA, or DIDS, and then treatment with ER–horse (Fig. 6f). The results showed that cell survival increased significantly after 2–APB pretreatment, providing further evidence that apoptosis was elicited by the CRAC channel activation after cellular uptake of ER–horse. Consistent with CCK–8 analysis (Fig. 6c), the flow cytometry results revealed that the treatment with ER–horse led to a significant

increase in the percentage of apoptotic tumor cells compared to those in the control groups (with apoptosis rates of 53.85% for ER–horse group, 13.76% for NC–ERVs group, 9.54% for ERVs group, 7.55% for NC group, 6.49% for siGRP94 group) (Fig. 6g).

Tumor homologous targetability and therapeutic efficacy in vivo. Inspired by the distinct therapeutic effects mediated by ER–horse in vitro, we systematically investigated its antitumor performance in vivo. Prior to this analysis, the in vivo biodistribution of ER–horse was inspected in a HepG2 cell xenograft model in BALB/c nude mice (Supplementary Fig. 10). Successful generation of this xenograft model was confirmed by visual observation of tumor nodules 14 d after the inoculation with HepG2 cells. HepG2 tumor–bearing nude mice were intravenously administered the same doses of ER–horse, siGRP94–RBCVs or siGRP94–CCVs labeled with the near–infrared dye DIR. Fluorescence imaging of the treatment groups was performed at designated time points (0, 4, 8, 12, 24, 36, and 48 h) to obtain an initial estimate of vesicle distribution (Supplementary Fig. 10a, c). The images showed that siGRP94–FITC was quickly cleared from the circulation and rarely reached the tumor site. Conversely, a strong and sustained (from 36–48 h) fluorescence signal was observed at tumor sites in mice injected with ER–horse, whereas there was negligible fluorescence at the tumor site at 48 h in the mice treated with the other vesicles. These results suggested that encapsulation by ERVs decreased the clearance of siGRP94 and prolonged its time in circulation and in vivo target residence time; these effects are beneficial for subsequent antitumor effects.

To intuitively analyze the distribution of fluorescence in different organs ex vivo intuitively, the mice in each group were euthanized after 48 h, and major organs (e.g., the heart, liver, spleen, lungs, and kidneys) and tumors were collected and subjected to fluorescence imaging to analyze vesicle accumulation. ER–horse accumulated in tumors to a significantly greater extent than the other three vesicle types (Supplementary Fig. 10b, d); these data demonstrated the strong tumor–targeting ability of ERVs, which showed enhanced binding to liver cancer cells and thus increased siGRP94 accumulation in tumors. The fluorescence intensities in liver and spleen were relatively high in all vesicle groups (ER–horse, siGRP94–RBCVs, and siGRP94–CCVs). We speculated that glycoproteins on biovesicles may be recognized by cognate receptors on cells within these organs, leading to accumulation of fluorescence signal, but the specific mechanism should be further assessed.

To confirm that ER–horse induced severe Ca^{2+} imbalance and ROS production at tumor site, frozen tumor sections from mice treated with PBS (control), siGRP94, ERVs, or ER–horse of 48 h were stained with Fluo–4 AM (calcium) and dihydroethidium (DHE, ROS). In comparison to the PBS, siGRP94 and ERV groups, the ER–horse group showed the stronger fluorescence intensities of Ca^{2+} and ROS in tumor sections, indicating that the large–scale Ca^{2+} influx and ROS production occurred in this group (Fig. 7a).

Then, immunohistochemistry (IHC) and histological analyses of tumor sections treated above were performed to evaluate preliminary indicators of the potential therapeutic efficacy of ER–horse. In ER–horse group, the levels of ERS marker protein GRP78 were clearly increased, but those of other ERS marker GRP94 were not, probably due to gene silencing by the delivered siGRP94. IHC results suggested

that ER–horse induced apoptosis by downregulating a protective UPR–related protein (GRP94) after triggering ERS, as indicated by the increased GRP78 expressions (Fig. 7b). In the hematoxylin and eosin (H&E) staining, tumors treated with ER–horse had the largest necrotic areas, whereas tumors in the siGRP94 group and ERV group were similar to those in the control group, with some indication of normal morphology (Fig. 7c). Sections of the major organs were also analyzed by H&E staining and negligible morphological damage of major organs was observed in any of the groups (Supplementary Fig. 11). Similar to H&E staining of tumors, significant green fluorescence indicating apoptotic cells was observed in the tumors incubated with ER–horse compared with from the other groups in terminal deoxynucleotidyl transferase dUTP nick–end labeling (TUNEL) staining assays, (Fig. 7d). Taken together, the findings indicated the potential of ER–horse to inhibit the growth of tumors derived from HepG2 cells.

To obtain further insight into the antitumor activity, body weight and tumor volume were measured to monitor the therapeutic efficacy (Fig. 7e and f). Balb/c nude mice bearing HepG2 tumors were tail vein injected with ER–horse, ERVs, siGRP94 or PBS (labeled as control group) every other day. Negligible body weight abnormalities were monitored, suggesting the low biological toxicity of these groups. A mild tumor volume variation was observed in ERVs and siGRP94, indicating their weak antitumor performances. As expected, ER–horse exhibited the remarkable inhibition of tumor growth, attributing to its homologous targetability and stress cascade capacity. Consistently, ER–horse led to the highest tumor growth inhibition rate (80.9%) among these groups, indicating that ER–horse drastically inhibited tumor growth (Fig. 7g). Moreover, the excised tumor with ER–horse incubation presented the smallest tumor size (Fig. 7h). H&E staining of tumor tissues also suggested that the ER–horse presented large necrotic regions when compared with the other control groups (Fig. 7i). Taken together, as the homologous biovesicles and stress cascade inducer, ER–horse enabled tumor–specific accumulation and eventually potentiated precise HCC nanotherapy harnessing biovesicle surface functions.

Conclusion

In summary, we constructed a homologous ER–horse boosting stress cascade for precise and potent HCC nanotherapy. The ER membrane endowed ER–horse with mannose, thus enabled homotypic recognition with MR on HepG2 cells. After recognition and binding, CRAC channels were activated by the coupling of Ca^{2+}–sensing STIM1 on ER–horse and Ca^{2+}–selective ORAI1 on HepG2 cells, causing Ca^{2+} influx to intracellular Ca^{2+} homeostasis disruption. Meanwhile, ER–horse facilitated the endosomal escape of siGRP94 through a highly efficient membrane fusion mechanism, and siGRP94 was released into the ER area without endosome destruction due to the reorganization of Endo–ERVs. With the entry of Ca^{2+} and the downregulation of GRP94 through siRNA–mediated gene silencing, ER–horse successfully triggered the stress cascade (Ca^{2+} homeostasis disruption–ERS–OS), and eventually achieved precise HCC nanotherapy. This work provides a novel and general strategy for construction of versatile ER membrane–based vesicles that can be used to trigger stress cascade with homologous targetability effects for therapy and may suit the needs of diverse biomedical applications.

Methods

Materials. All materials can be found in the accompanying Supplemental Information file.

Cell culture. HepG2 human liver cancer cells, SMMC–7721 human liver cancer cells (hereinafter referred to as 7721 cells), L02 human liver cells, SK–BR–3 human breast cancer cells, MCF 10A human breast epithelial cell cells, and human RBCs were provided by the Chinese Academy of Sciences Cell Bank and Chongqing Traditional Chinese Medicine Hospital. The cells were cultured with DMEM/F12 supplemented with 10% fetal bovine serum, 100 units/mL penicillin, and 100 μg/mL streptomycin at 37°C in a humidified atmosphere of 5% CO_2.

Detailed synthesis procedure of ER–horse. The ER membrane was isolated with an ER isolation kit according to the manufacturer's protocol. Briefly, the cells were washed with 10 volumes of PBS (0.01 M, pH 7.4) and centrifuged at 600 × g for 5 min three times, and the supernatant was removed by aspiration. Then, the packed cell volume (PCV) was measured, and the cells were suspended in a volume of 1× Hypotonic Extraction Buffer (an aliquot of 10× Hypotonic Extraction Buffer was diluted 10–fold with water. Just before use, Protease Inhibitor Cocktail for mammalian cells was added to the 1× Hypotonic Extraction Buffer at a concentration of 1% (v/v)) equivalent to 3 times the PCV and incubated for 20 min at 4°C, which allowed the cells to swell. Next, the cells were centrifuged at 600 × g for 5 min, the supernatant was removed by aspiration, and the "new" PCV was measured. Then, a volume of 1× Isotonic Extraction Buffer (created by aseptically removing an aliquot of 5× Isotonic Extraction Buffer and diluting it 5–fold with water. The 1× Isotonic Extraction Buffer was kept at 4°C before use. Just before use, Protease Inhibitor Cocktail for mammalian cells was added to the 1× Isotonic Extraction Buffer at a concentration of 1% (v/v)) equivalent to 2 times the "new" PCV was added, and the mixture was transferred to a 7 mL Dounce homogenizer. The homogenizer was used to break the cells with 10 strokes. Finally, the homogenate was centrifuged at 1,000 × g for 10 min at 4°C. The thin floating lipid layer was carefully removed by aspiration. The supernatant was transferred to another centrifuge tube using a pipette, and the pellet was discarded. The supernatant was centrifuged at 12,000 × g for 15 min at 4°C. The thin floating lipid layer was carefully removed by aspiration. The supernatant was transferred to another tube using a pipette, and the pellet was discarded. The obtained product was stored at 4°C. According to the calculations, 1.2×10^{-2} mg of ER was extracted per disk. After mixing with siGRP94 (dissolved in 0.01 M PBS; the final concentration was 10 μM), the suspension was kept at 4°C and extruded five times through a polycarbonate filter of 1.0 μm, five times through a polycarbonate filter of 0.5 μm, and five times through a polycarbonate filter of 0.2 μm using an Avanti Hand Extruder (Avanti Polar Lipids). The final products were characterized by TEM, DLS, CLSM and WB.

Immunofluorescence. Cells (5×10^5) were overlaid on sterilized coverslips in 24–well plates with 2 mL of medium. After 24–48 h, the cells were washed three times with 1× PBS and then fixed with 4% (v/v) paraformaldehyde for 10 min in the dark. The cells were then permeabilized with 0.1% (v/v) Triton X–100 for 10 min and subsequently blocked using 2% (w/v) bovine serum albumin for 1 h. The cells were incubated with a CNX primary antibody at a 1:200 dilution. Cells were washed three times with 1× PBS

and then stained with goat anti–rabbit IgG–DyLight 549 (1:400 dilution) and Conanavalin A–FITC (Con A–FITC, 1 μg/mL, containing 1 mg/mL Ca^{2+} and Mn^{2+}) for 60 min. DAPI (10 μg/mL) was used as the nuclear stain. A Zeiss LSM510 confocal microscope was used to visualize the cells under a 40× /1.3 oil DIC M27 objective. ImageJ and Leica software were used for image analysis.

Characterization of ER–horse. ER–horse (1.2×10^{-2} mg/mL, quantified by ERVs) and ER (treated with 10 μM siGRP94, 1.2×10^{-2} mg/mL ERVs and 1.2×10^{-2} mg/mL ER–horse for 0 h and 36 h) were characterized by using TEM. Briefly, samples were examined using a Jeol JEM–2100 transmission electron microscope operated at 200 kV. The samples were applied to copper grids for 2 min. The samples were then air–dried and stained using a 2% w/v uranyl acetate solution (Electron microscopy services). A NanoSight NS300 machine (Malvern Instruments, Malvern, UK) equipped with a sample chamber and 640 nm laser was used to analyze the size distribution of ER–horse. ERVs samples (1.2×10^{-2} mg/mL) were disaggregated using a needle and syringe before injection into the NanoSight sample cuvette. The frame rate was 30 frames per second. Data analysis was performed using NanoSight NTA 3.2 software.

WB analysis was performed to identify the protein profiles of ER–horse. Briefly, equal amounts of the total proteins from different samples quantified with a BCA Protein Assay Kit were added to a 10% SDS–polyacrylamide gel electrophoresis (SDS–PAGE) gel to separate proteins of different molecular weights. Subsequently, the gel was stained with Coomassie brilliant blue and imaged. For the WB assay, the proteins on the gel were then transferred to a polyvinylidene fluoride membrane, and then the membrane was blocked with 5% skimmed milk and incubated with primary antibodies against CNX, CRT, and STIM1. The membrane was incubated with an anti–goat IgG secondary antibody corresponding to the primary antibodies before imaging was performed with ECL Western Blotting Substrate.

The integrative hybrid nanostructure of ER–horse was further determined by the colocalization of the ER membrane and siGRP94. Briefly, siGRP94 was labeled with FITC, and the ER membrane was labeled with antibodies (an anti–CNX primary antibody and a DyLight 549–labeled secondary anti–rabbit IgG antibody). Then, two–fluorescence dye–labeled ER–horse (FITC–siGRP94: 10 μM; ERVs: 1.2×10^{-2} mg/mL) was assembled. Four microliters of ER–horse was dropped onto the slide, and fluorescence images were obtained using a Leica SP8 CLSM (Wetzlar, Germany) at different excitation wavelengths (DyLight 549: 549 nm; FITC: 488 nm).

For size distribution evaluation, nanoparticle tracking analysis (NTA) was performed with a NanoSight NS300 (Malvern, UK) equipped with a 405 nm laser and an sCMOS camera. Resuspended ER–horse (1.2×10^{-2} mg/mL, quantified by ERVs) were diluted 50–fold in filtered PBS to achieve a final concentration of 2.4×10^{-4} mg/mL. The capture length was 60 s with the camera level set to 14 and the detection threshold set to 3. An image of filtered PBS was taken to verify that the diluent had no particles. A total of 1498 frames were captured and analyzed. NTA 3.2 Dev Build 3.2.16 software (Malvern, UK) was used for capturing and data analysis.

The hydrodynamic size and zeta potential of ERVs (1.2×10^{-2} mg/mL, quantified by ERVs), ER–horse (1.2×10^{-2} mg/mL, quantified by ERVs) and siGRP94 (10 μM) diluted in PBS (0.01 M, pH 5.5, pH 6 and pH 7.4) were measured by DLS using a Malvern Zetasizer Nano ZS. The particle size versus the number of particles per mL and the average zeta potential were plotted using Origin 9.0 software (average of 3 biological replicates).

To investigate the encapsulation of siGRP94 in ER–horse, the protective effect of ER–horse on siGRP94 in serum–containing medium was detected. The ER–horse (siGRP94: 10 μM, labeled with FITC) and siGRP94 (10 μM, labeled with FITC) were incubated with DAPI–labeled HepG2 cells for 1 h in serum–containing medium (containing 10% FBS). The cells were fixed with 4% paraformaldehyde. The protective effect of the ERVs was analyzed by CLSM following mounting with antifade polyvinylpyrrolidone mounting medium.

Homologous–targeting Ability Of Er–horse

Determination of the abundance of MR in different cell lines. To explore the homologous targeting ability of ER–horse in different cell lines, it was necessary to detect the abundance of MR on the cell membranes. Briefly, different cell types (HepG2 liver cancer cells, 7721 liver cancer cells, L02 liver normal cells, MCF 10A normal breast epithelial cells and SK–BR–3 breast cancer cells) were seeded into 24–well plates (1.0×10^4 cells per well) and cultured overnight. The cells were then blocked in 5% serum for 30 min and probed with primary antibodies (CD206, diluted at 1:400) overnight at 4°C. After primary antibody incubation, the cells were washed 3 times with PBST (0.01 M PBS containing 0.05% (v/v) Tween–20) and incubated with the appropriate DyLight 549–conjugated secondary antibody (anti–mouse IgG antibody, diluted at 1:400) for 1 h at room temperature. Then, the cells were washed 3 times with PBST, and the nuclei were counterstained with DAPI. Photographs were taken with a confocal microscope (FV1000, Olympus, Japan) and analyzed using LAS X software.

Interaction of mannose and MR. ER–horse was incubated with Con A–FITC (10 μg/mL) at 37°C for 1 h in the dark and added to HepG2 cells. After incubation for 30 min, the HepG2 cells were fixed with 4% paraformaldehyde and then labeled with a primary antibody against CD206 and a secondary antibody conjugated with DyLight 549. The nuclei were counterstained with DAPI. CLSM (Olympus FV 1000) was used to observe the fluorescence signals. Pearson's coefficient was calculated using the JACoP plugin of ImageJ 1.46r software.

Blocking with free mannose. To block the capturing effect of MR on the surfaces of HepG2 cells, cells were incubated with excessive free mannose. First, HepG2 cells were seeded into 24–well plates (1.0×10^4 cells per well) and cultured overnight. The cells were then incubated with free mannose (2 mg/mL) at 37°C for 1 h. Then, the blocked cells were incubated with ER–horse (working concentration 10 μM) at 37°C for 30 min, washed with PBS to remove the unbound free mannose and used for the indicated

assays. The cells were fixed with 4% paraformaldehyde. The ability of HepG2 cells to capture ER–horse was analyzed by CLSM following mounting with antifade polyvinylpyrrolidone mounting medium.

Comparison of the homologous targeting of ER–horse to different cells. ER–horse was incubated with Con A–FITC (10 μg/mL) at 37°C for 1 h in the dark. Cells (including HepG2, 7721, and L02 cells) were incubated with ER–horse (labeled with FITC) for 0, 2, 5, 10, and 30 min. The cells were fixed with 4% paraformaldehyde. The homologous targeting effect of ER–horse was analyzed by CLSM following mounting with antifade polyvinylpyrrolidone mounting medium.

Interaction of STIM1 and ORAI1. ER–horse was labeled with a primary antibody against STIM1 (diluted at 1:100) and a secondary antibody conjugated to DyLight 549 (anti–rabbit IgG antibody, diluted at 1:400) and added to HepG2 cells. After incubation for 30 min, the HepG2 cells were fixed with 4% paraformaldehyde and then labeled with a primary antibody against ORAI1 (diluted at 1:100) and a secondary antibody conjugated with Cy5 (anti–mouse IgG antibody, diluted at 1:400). The nuclei were counterstained with DAPI. CLSM (Olympus FV 1000) was used to observe the fluorescence signals. Pearson's coefficient was calculated using the JACoP plugin of ImageJ 1.46r software.

Uptake Of Er–horse In Hepg2 Cells

Homologous Fusion of ER–horse with the PM in HepG2 cells. HepG2 cells were seeded into 24–well plates (1.0×10^4 cells per well) and cultured at 37°C for 24 h. The cells were incubated with Hoechst 33258 (10 μg/mL, blue) and DIL (10 μM, green) for approximately 15 min to stain the cell nucleus and PM. Afterward, the cells were washed twice using PBS and then incubated with ER–horse (labeled with Con A–FITC, final concentration of 1.2×10^{-2} mg/mL, red) for another 5 min. Finally, the cells were washed, incubated with fresh medium and then observed under a CLSM every 5 min.

Fusion of ERVs and endosomes. HepG2 cells were seeded into 24–well plates (1.0×10^4 cells per well) and cultured at 37°C for 24 h. The cells were incubated with DAPI (10 μg/mL, blue) for 5 min. Afterward, the cells were washed twice using PBS and then incubated with FITC–labeled dextran (1 mg/mL, green) and ER–horse (red, labeled with DIL, final concentration of 1.2×10^{-2} mg/mL) for 1 h. Finally, the cells were washed, incubated with fresh medium and then observed under a CLSM.

Transport and release of siGRP94 by Endo–ERVs. HepG2 cells were seeded into 24–well plates (1.0×10^4 cells per well) and cultured at 37°C for 24 h. Afterward, the cells were washed twice using PBS and incubated with ER–horse (the siGRP94 was labeled with FITC, final concentration of 10 μM) for 0.5–1.5 h. Then, after washing twice with 1× PBS, the cells were fixed with 4% (v/v) paraformaldehyde for 10 min in the dark, permeabilized with 0.1% (v/v) Triton X–100 for 10 min and subsequently blocked using 2% (w/v) bovine serum albumin for 1 h. The cells were incubated with primary antibodies (EEA1 and CNX, diluted 1:200) and secondary antibodies (anti–mouse IgG–DyLight 649, purple; anti–rabbit IgG(H + L)–DyLight 549, red). The nuclei were counterstained with DAPI. CLSM (Olympus FV 1000) was used to observe the fluorescence signals.

Endosomal escape process and mechanism. HepG2 cells were seeded into 24–well plates (1.0×10^4 cells per well) and cultured at 37°C for 24 h. The cells were incubated with Hoechst 33258 (10 μg/mL) for approximately 15 min to stain the cell nucleus. Afterward, the cells were washed twice using PBS and then incubated with Alexa 647–labeled dextran (1 mg/mL, purple) and ER–horse (the siGRP94 was labeled with FITC, green; the ERVs were labeled with DIL, red; final concentration of 10 μM, quantified by siGRP94) for 1 h at 37°C. Finally, the cells were washed, incubated with fresh medium and then observed by CLSM with a Leica SP8 every 15 min.

Mechanism Of Induced Stress Cascade

Determination of the intracellular Ca^{2+} concentration and ROS production in the cells. HepG2/L02/7721 cells were incubated with ER–horse (1.2×10^{-2} mg/mL), siGRP94–RBCVs (10 μM), siGRP94–CCVs (10 μM), ERVs (1.2×10^{-2} mg/mL), NC–ERVs (10 μM), or siGRP94 (10 μM) for 0–12 h. The levels of $[Ca^{2+}]$ i were measured with Fluo–4 AM (excitation wavelength of 488 nm and emission wavelength of 525 nm), a visible–wavelength Ca^{2+} probe. The intracellular generation of ROS was inspected with DHE (excitation wavelength of 435 nm and emission wavelength of 610 nm). DHE is the most commonly used fluorescent probe to detect the levels of superoxide anions in cells. The dye (containing 5 μM DHE and 5 μM Fluo–4 AM) was added to the cells, and the cells were incubated for 1 h at 37°C under 5% CO_2 in the dark according to the protocols. Then, the cells were washed three times with PBS (pH 7.4). The nuclei were counterstained with DAPI. Fluorescence was measured by CLSM and flow cytometric analysis.

Determination of the intracellular Ca^{2+} concentration and the production of ROS in HepG2 cells by incubation with ER–horse after pretreatment with different drugs. Before incubation with ER–horse, HepG2 cells were pretreated with different drugs that affect intracellular Ca^{2+} homeostasis, including BAPTA (12.5 μM), 2–APB (25 μM), and DIDS (30 μM). After 20 min of pretreatment at 37°C, the HepG2 cells were incubated with ER–horse (1.2×10^{-2} mg/mL) for 1 h at 37°C. The levels of Ca^{2+} and ROS were measured with Fluo–4 AM and DHE, respectively. Then, the cells were washed three times with PBS (pH 7.4). The nuclei were counterstained with DAPI. Fluorescence was measured by CLSM and flow cytometric analysis.

Protein extraction and WB analysis. Cells were washed three times with cold PBS and lysed on ice using 100 μL of RIPA lysis reagent supplemented with 2 μL of PMSF for 30 min. Cell debris was removed by centrifugation at 14,000 × g for 20 min at 4°C. The protein concentration was measured by BCA assay. The clarified protein lysates from each experimental condition were boiled for 5 min. Protein samples (30 μg) were subjected to 10% (SDS–PAGE and transferred onto polyvinylidene difluoride membranes. After blocking with 5% nonfat milk in 1× TBST containing 0.05% Tween–20 for 2 h at room temperature, the membranes were incubated with specific primary antibodies overnight at 4°C. Anti–mouse IgG and anti–rabbit IgG were used as secondary antibodies. Specific proteins were detected with enhanced chemiluminescence reagent. The antibodies used were as follows: anti–GRP94 (1:1000), anti–GRP78

(1:1000), anti–Bcl–2 (1:1000), anti–Bax (1:1000), anti–Casepase–12 (1:1000), anti–CHOP (1:1000), anti–TRAF2 (1:1000) and anti–Cl–casepase3 (1:1000).

Analysis of cell survival via CLSM. HepG2/L02/7721 cells were seeded into 24–well plates (1.0×10^4 cells per well) and cultured at 37°C for 24 h. Afterward, the cells were washed twice using PBS and incubated with ER–horse (10 μM) for 36 h before being centrifuged at 1,000 × g for 5 min. Then, the cell culture medium was aspirated, and the pellet was washed twice using PBS and incubated with 200 μL of staining solution (containing 10 μL of PI) for 20 min at room temperature. After washing twice with 1× PBS, the apoptosis results were observed by CLSM (excitation at 535 nm and emission at 617 nm)

Cytotoxicity assay. The cytotoxicity of these formulations was evaluated using a CCK–8 assay. HepG2/L02/7721 cells were seeded in 96–well plates at 5,000 cells per well and cultured overnight. The cells were then incubated with different formulations in the different pretreatments (siGRP94, ERVs, ER–horse, siGRP94–RBCVs, siGRP94–CCVs) for 0–36 h. PBS diluted with DMEM was used for the NC group. CCK–8 reagent was added to each well (10 μL per well), and the cells were incubated for another 4 h. After incubation, the absorbance at 490 nm was measured by a microplate reader (BioTek Synergy H1, USA). The cell viability was calculated.

Flow cytometric analysis of apoptosis. Cells incubated with different formulations for 36 h, including siGRP94, NC, ERVs, NC–ERVs, and ER–horse (1.2×10^{-2} mg/mL), were harvested, washed in cold PBS, centrifuged three times at 1,000 × g for 5 min and then resuspended in PBS. A flow cytometry assay was performed using double staining (PI and annexin V) at the Academy of Life Sciences (Chongqing Medical University, China).

Animal Experiments

In vivo biodistribution. Four–week–old male BALB/c–nude mice purchased from the Laboratory Animal Services Center of Chongqing Medical University were maintained under pathogen–free conditions. All procedures for the mouse experiments were approved by the Ethics Committee of Chongqing Medical University. The mice were subcutaneously inoculated with a HepG2 cell suspension (1.0×10^6 cells in 100 μL of PBS) and maintained until measurable tumor masses (2–3 mm) formed. To investigate the tumor–targeting effect and distribution of ER–horse in tumor tissues, ER–horse (labeled with DIR), siGRP94–RBCVs (labeled with DIR), siGRP94–CCVs (labeled with DIR), and siGRP94–FITC were intratumorally injected into mice via the tail vein at a siGRP94 concentration of 1 mM per mouse. At certain times post–injection, the mice were anesthetized with isoflurane, and fluorescence images of the mice were acquired using an in vivo imaging system (IVIS Spectrum; PerkinElmer, USA). After 48 h, the mice were sacrificed, and the tumors together with other major organs (heart, liver, spleen, lungs, and kidneys) were collected for ex vivo imaging. The fluorescence signals from different organs were analyzed with IVIS software.

Tissue section Ca^{2+} and ROS staining. To assess the increases in Ca^{2+} and ROS in vivo, the tumor–bearing mice were then randomly divided into 4 groups (the PBS group, siGRP94 group, ERV group, and

ER–horse group). The treatment formulations were peritumorally injected. The mice were euthanized after 36 h, and their tissues were dissected. The tissues were snap–frozen in liquid nitrogen, embedded in O.C.T. compound, and cut into frozen sections (10 μm). The sections were stained with Fluo–4 AM and DHE and then imaged by confocal microscopy.

IHC study and histological analysis. Immunostaining was completed on paraffin–embedded tumor tissues (in the PBS group, siGRP94 group, ERV group, and ER–horse group). A GRP94 antibody (1:1000) and a GRP78 antibody (1:1000) were used in IHC with the streptavidin peroxidase–conjugated method. The sections were visualized under a microscope at 400× magnification. The tumors and other major organs (heart, liver, spleen, lungs, and kidneys) were sectioned for H&E staining. Finally, the tumors were stained with TUNEL and imaged by confocal microscopy.

In vivo antitumor efficacy using a hepatocellular carcinoma tumor Model. The antitumor mechanism was studied based on the following experiments. BALB/c mice were injected subcutaneously with 1×10^6 HepG2 tumor cells in the right flank to prepare the tumor model. When the tumor size reached ~ 100 mm^3, mice were randomly divided into 4 groups (n = 4) and injected peritumorally with PBS (labeled as Control group), siGRP94 group, ERVs group, and ER–horse group at a siGRP94 dose (0.5 mg/kg) and ERVs dose (1.2 mg/mL) in 150 μL of PBS buffer once every 2 days. All the mice were administered seven consecutive injections, the tumor growth was monitored by measuring perpendicular diameters using a calliper, and tumor volume was calculated as follows: $V = L \times W^2/2$, where W and L represent the shortest and longest diameters, respectively. The tumor volumes and mice body weights were monitored every day. Two days after the last injection, the animals were sacrificed to harvest tumors and the image was captured by camera (Nikon D5100, Japan) and weighted. The pathological changes of tumors were analyzed by H&E staining. All animal testing and research were complied with the relevant ethical regulations. All animal procedures were approved by the Research Ethics Committee of Chongqing Medical University (reference number: 2022-k54).

Statistical Analysis. All data are represented as mean ± standard deviation (SD) (n = 3), and statistical differences between two groups were determined using unpaired two–tailed Student's t–test (*$p < 0.05$, **$p < 0.01$, and ***$p < 0.001$). Statistical significance was set at $p < 0.05$.

Reporting Summary. Further information on research design is available in the Nature Research Reporting Summary linked to this article.

Data Availability Statement

The data that support the findings of this study are available from the corresponding author upon reasonable request.

References

1. Schroder, M. & Kaufman, R.J. ER stress and the unfolded protein response. *Mutat. Res*. **569**, 29–63 (2005).

2. Shen, X., Zhang, K. & Kaufman, R.J. The unfolded protein response: a stress signaling pathway of the endoplasmic reticulum. *J. Chem. Neuroanat*. **28**, 79–92 (2004).

3. Rao, R.V., Ellerby, H.M. & Bredesen, D.E. Coupling endoplasmic reticulum stress to the cell death program. *Cell Death Differ*. **11**, 372–380 (2004).

4. Breckenridge, D.G. et al. Regulation of apoptosis by endoplasmic reticulum pathways. *Oncogene*. **22**, 8608–8618 (2003).

5. Hetz, C., Chevet, E. & Harding, H. P. Targeting the unfolded protein response in disease. *Nat. Rev. Drug Discovery* **9**, 12, 703719 (2013).

6. Kaufman, R. J. Orchestrating the unfolded protein response in health and disease. *J. Clin. Invest.* **110**, 1389–1398 (2002).

7. Wang, M. & Kaufman, R. J. The impact of the endoplasmic reticulum proteinfolding environment on cancer development. *Nat. Rev. Cancer*. **14**(9), 581597 (2014).

8. Walter, P. & Ron, D. The unfolded protein response: from stress pathway to homeostatic regulation. *Science* **334**, 1081–1086 (2011).

9. Lee, A. H., Iwakoshi, N. N., Anderson, K. C. & Glimcher, L. H. Proteasome inhibitors disrupt the unfolded protein response in myeloma cells. *Proc. Natl Acad. Sci. USA* **100**, 9946–9951 (2003).

10. Schroder, M. & Kaufman, R. J. The mammalian unfolded protein response. *Annu. Rev. Biochem.* **74**, 739–789 (2005).

11. Garg, A. D., Maes, H., van Vliet, A. R. & Agostinis, P. Targeting the hallmarks of cancer with therapyinduced endoplasmic reticulum (ER) stress. *Mol. Cell. Oncol*. **2**(1), 975089 (2015).

12. Ojha, R. & Amaravadi. R. K. Targeting the unfolded protein response in cancer. *Pharmacol. Res.* **120**, 258266 (2017).

13. Healy, S. J. M. et al. Targeting the endoplasmic reticulumstress response as an anticancer strategy. *Eur. J. Pharmacol*. 234246 (2009).

14. Walter, P. & Ron, D. The unfolded protein response: from stress pathway to homeostatic regulation. *Science* **334**, 10811086 (2011).

15. Hetz, C., Zhang, K. & Kaufman, R. J. Mechanisms, regulation and functions of the unfolded protein response. *Nat. Rev. Mol. Cell Biol*. **21**, 421–438 (2020).

16. Cao, B., Li, J. & Mao, X. Dissecting Bortezomib: Development, Application, Adverse Effects and Future Direction. *Curr. Pharm. Des*. **19**, 31903200 (2013).

17 Peinelt, C. et al. Amplification of CRAC current by STIM1 and CRACM1 (Orai1). *Nat. Cell Biol*. **8**, 771–773 (2006).

18 Waldherr, L., Tiffner, A., Mishra, D., Sallinger, M. & Schindl, R. Blockage of store–operated Ca^{2+} influx by synta66 is mediated by direct inhibition of the Ca^{2+} selective Orai1 pore. *Cancers* **12**, 2876 (2020).
19. Luik, R. B., Wang, B., Prakriya, M. & Wu, M. Oligomerization of STIM1 couples ER calcium depletion to CRAC channel activation. *Nature* **454**, 538–542 (2008).

20. Saheki, Y. & De Camilli, P. Endoplasmic reticulum–plasma membrane contact sites. *Annu. Rev. Biochem*. **86**, 659–684 (2017).

21. Loncke, J. et al. Balancing ER–mitochondrial Ca fluxes in health and disease. *Trends Cell Biol*. **31**, 598–612 (2021).

22. Gómez–Valadés, A. G. et al. Mitochondrial cristae–remodeling protein OPA1 in POMC neurons couples Ca homeostasis with adipose tissue lipolysis. Cell Metab. **33**, 1820–1835 (2021).

23. Wang, C. et al. Surfactin–induced apoptosis through ROS–ERS–Ca^{2+}–ERK pathways in HepG2 cells. *Cell Biochem. Biophys*. **67**, 1433–1439 (2013).

24. Sari, F. R. et al. Sex differences play a role in cardiac endoplasmic reticulum stress (ERS) and ERS–initiated apoptosis induced by pressure overload and thapsigargin. *Cardiovasc. Pathol*. **20**, 281–290 (2011).

25. Wang, R. et al. Total saponins of aralia elata (Miq) seem alleviate calcium homeostasis imbalance and endoplasmic reticulum stress–related apoptosis induced by myocardial ischemia/reperfusion injury. *Cell Physiol. Biochem*. **50**, 28–40 (2018).

26. Nakano, H. et al. Reactive oxygen species mediate crosstalk between NF–kappaB and JNK. *Cell Death Differ*. **13**, 730–737 (2006).

27. Liu, H., Dai, L., Wang, M., Feng, F. & Xiao, Y. Tunicamycin induces hepatic stellate cell apoptosis through calpain–2/Ca–dependent endoplasmic reticulum stress pathway. Front. *Cell Dev. Biol*. **9**, 684857 (2021).

28. Veit, C., König, J., Altmann, F. & Strasser, R. Processing of the t erminal alpha–1,2–linked mannose residues from oligomannosidic N–glycans is critical for proper root growth. *Front. Plant Sci*. **9**, 1807 (2018).

29. Von Figura, K., Gieselmann, V. & Hasilik, A. Mannose 6–phosphate–specific receptor is a transmembrane protein with a C–terminal extension oriented towards the cytosol. *Biochem. J*. **225**, 543–

547 (1985).

30. Guan, C. et al. Glycosylated liposomes loading carbon dots for targeted recognition to HepG2 cells. *Talanta* **182**, 314–323 (2018).

31 Jiang, M. et al. Preparation of CdSe QDs–carbohydrate conjugation and its application for HepG2 Cells labeling. *B. Korean Chem. Soc*. **33**, 571–574 (2012).

32. Gai, X., Tu, K., Lu, Z. & Zheng, X. MRC2 expression correlates with TGFβ1 and survival in hepatocellular carcinoma. *Int. J. Mol. Sci*. **15**, 15011–15025 (2014).

33. Das, R. & Mohapatra, S. Highly luminescent, heteroatom–doped carbon quantum dots for ultrasensitive sensing of glucosamine and targeted imaging of liver cancer cells. *J. Mater. Chem. B* **5**, 2190–2197 (2017).

34. Alfadda, A. A. & Sallam, R. M. Reactive oxygen species in health and disease. *J. Biomed. Biotechnol.* **2012**, 936486 (2012)

35. Luk, B. & Zhang, L. Cell membrane–camouflaged nanoparticles for drug delivery. *J. Control. Release* **220**, 600–607 (2015).

Declarations

Acknowledgements

The authors acknowledge financial support from the projects of National Science and Technology Major Project of the Ministry of Science and Technology of China (2018ZX10732202), the National Natural Science Foundation of China (82002254, 81873972 and 81873980), the Natural Science Foundation of Chongqing (cstc2021jcyj–msxmX0119), the Chongqing Science Fund for Distinguished Young Scholars (cstc2019jcyjjqX0028), the Foundation for Innovative Research Groups of Chongqing Higher Education Institutions (CXQT20013), and Chongqing Medical University Graduate Talent Training Program (BJRC202023).

Author Contributions

X. T. B, N. K. F and M. L contributed equally to this study. W. C, S. Q. L and F. Z. S designed and supervised the study. X. T. B, N. K. F and M. L performed the major experiments. D. B. H, J.L, and X. Y. L performed the experiments. L. S. K and S. J. D wrote the paper. All authors read and approved the final manuscript.

The manuscript was written through contributions of all authors. All authors have given approval to the final version of the manuscript.

Competing Interest

The authors declare no conflict of interest.

Additional information

Supporting Information The online version contains supplementary material available at: http://www.xxx,xxx.

Correspondence and requests for materials should be addressed to Wei Cheng, Siqiao Li or Fangzhou Song.

Peer review information Nature Communications thanks xxx and the other, anonymous, reviewer(s) for their contribution to the peer review of this work. Peer reviewer reports are available.

Reprints and permission information is available at http://www.nature.com/reprints

Publisher's note Springer Nature remains neutral with regard to jurisdictional claims in published maps and institutional affiliations.

Figures

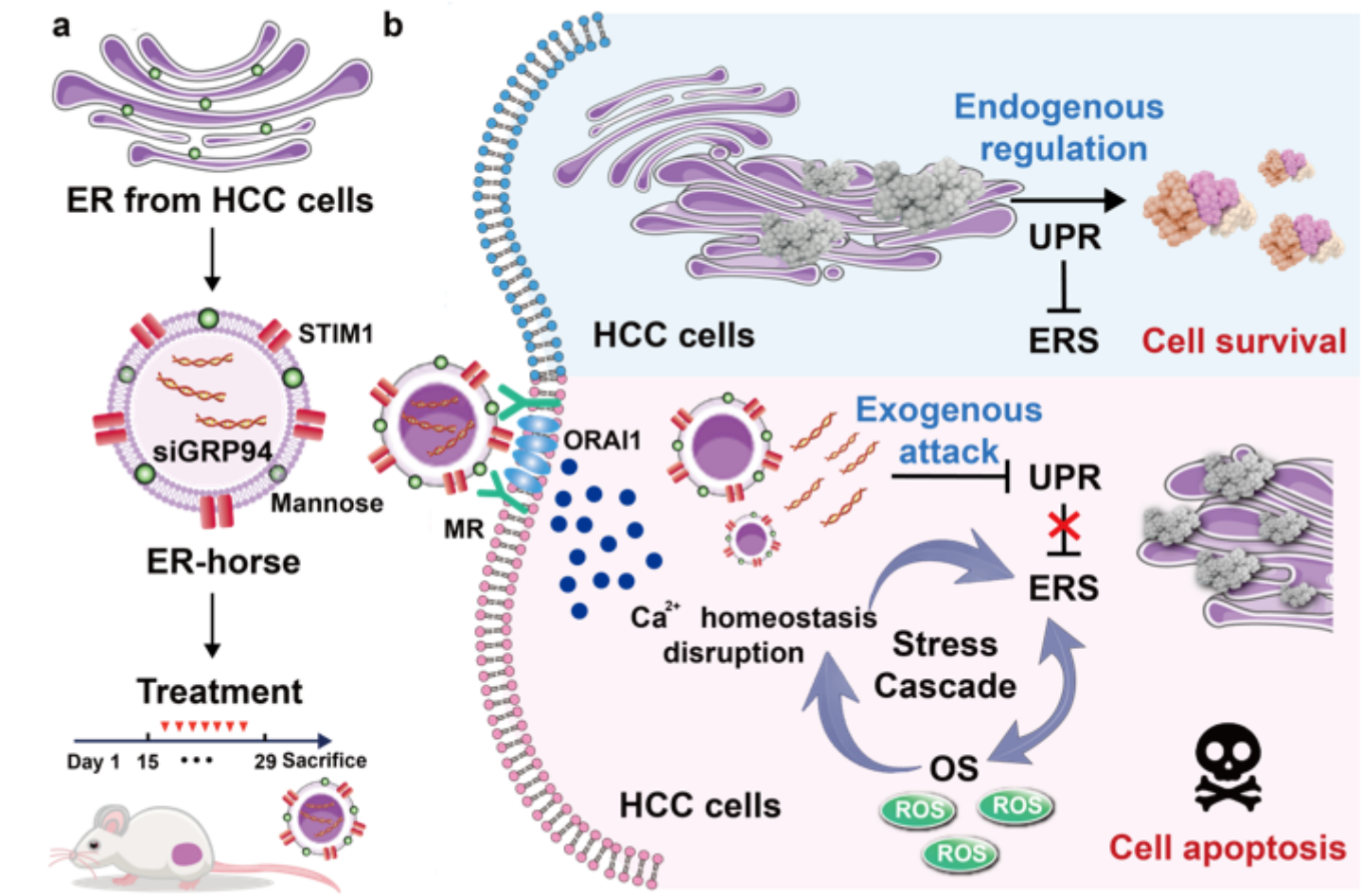

Figure 1

An ER–horse detonating stress cascade for hepatocellular carcinoma nanotherapy. a Description of the construction of the ER–horse and schematic representation of HCC model establishment and therapy process of ER–horse. **b** The two different fates of HCC cells with the treatment of ER-horse (below) or not (top).

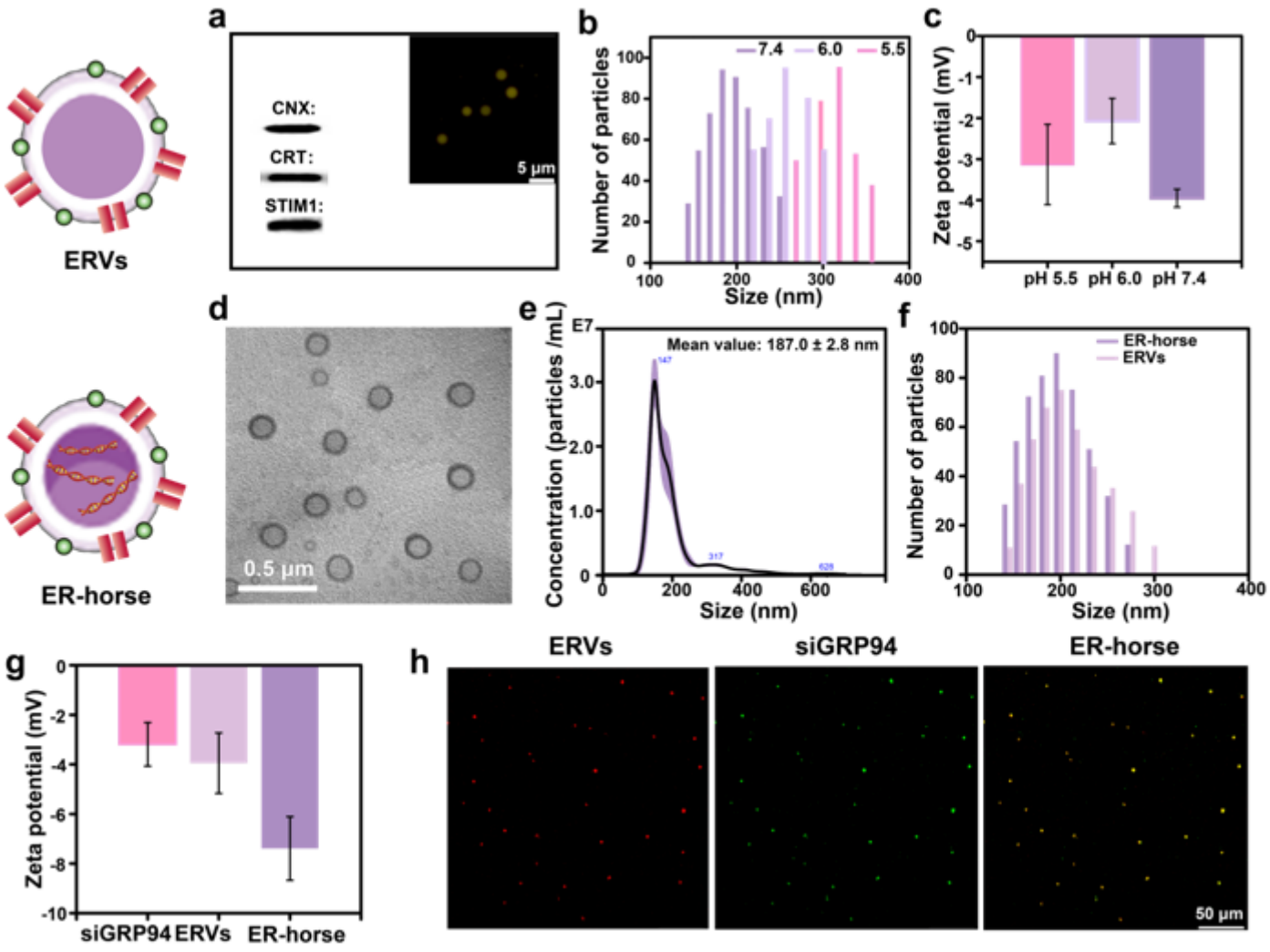

Figure 2

Production and characterization of ER–horse. **a** WB analysis of ER membrane proteins in the ERVs and a fluorescent image (upper right) of mannose (marked by Con A–FITC) on the ERVs extruded 25 times through a 2.0–μm polycarbonate filter. Scale bar = 5 μm. **b** Size distribution and **c**zeta potential of ERVs at pH 7.4, pH 6.0 and pH 5.5. **d** TEM images of ER–horse. Scale bar = 0.5 μm. **e** Mean value and size distribution determined by NanoSight NTA (left) of ER–horse and **f** DLS (right) of ERVs and ER–horse. The NTA data show the mean ± SD of three biological replicates and the concentration (data listed in the manuscript) of ER–horse. DLS data show the size distribution of ER–horse and ERVs. **g** Zeta potential of siGRP94, ERVs and ER–horse. **h** Simulation analysis of the integrated structure of ER–horse detected by CLSM, in which the ER membrane and siGRP94 were labeled with DiO and FITC, respectively. The data are expressed as the mean ± SD (n = 3).

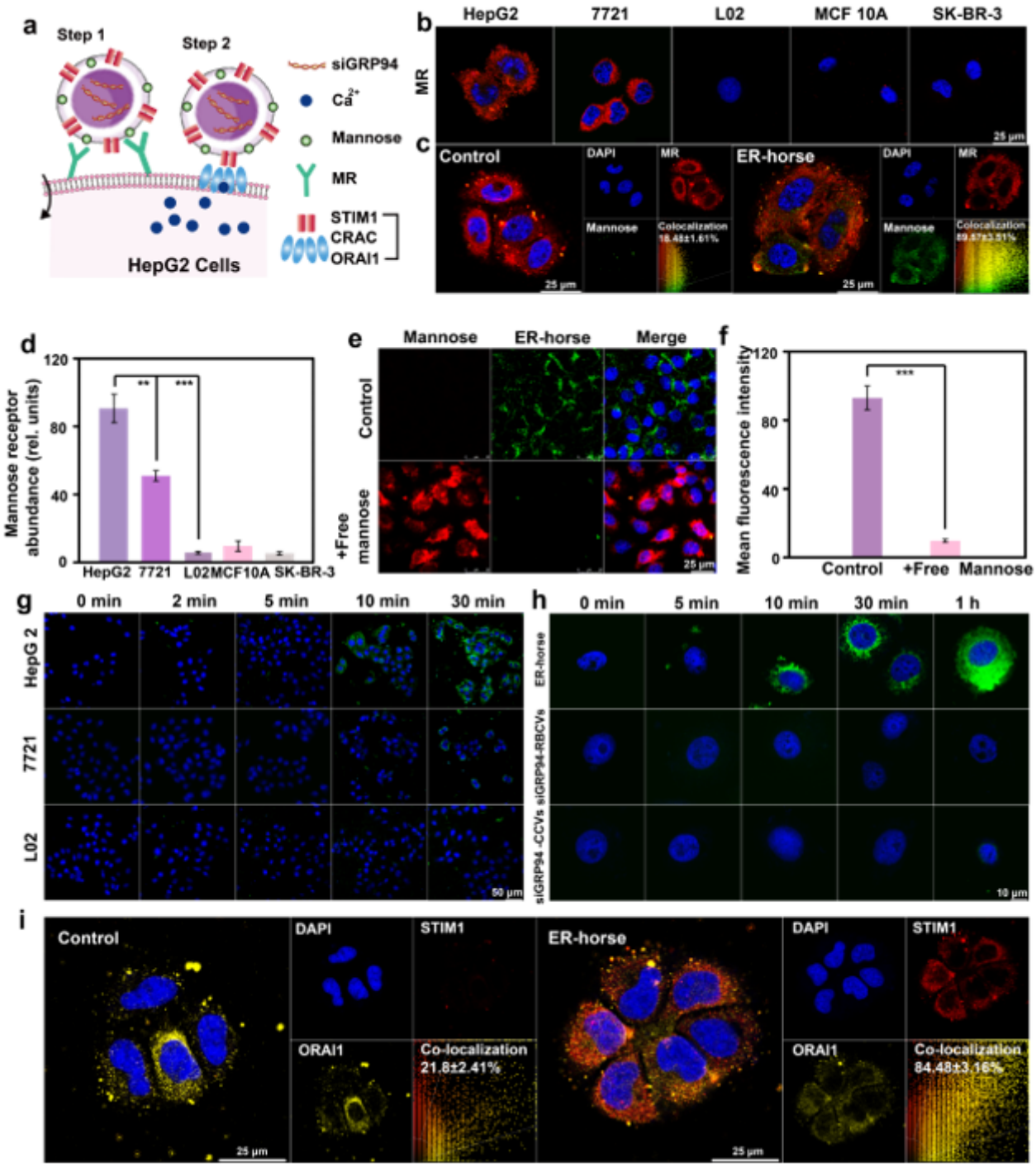

Figure 3

Cellular uptake of ER–horse. a Schematic diagram of the coupling of STIM1 on ER–horse to ORAI1 on the HepG2 cell membrane. **b**Determination of the abundance of MR (marked by anti–CD206) in different cell lines (HepG2, 7721, L02, MCF 10A and SK–BR2). **c** Interaction of mannose (green, marked by Con A–FITC) and MR (red). The group marked “Control” was treated without ER–horse. The group marked “ER–horse” was treated with 10 μM ER–horse for 30 min. The co–localization ratio was calculated by Pearson’s correlation coefficient. **d** Quantitative comparison of the abundance of MR in different cell lines by fluorescence intensity. **e** Cellular uptake of ER–horse(green, marked by Con A–FITC) before and after

blocking with free mannose (red, marked by Cy5). **f** Quantitative comparison of the cellular uptake effect of ER–horsebefore and after blocking with free mannose. **g** Comparison of the homologous targeting of ER–horse to different cells in 0–30 min (HepG2, 7721, L02). **h** Comparison of the homologous targeting of different siGRP94 vesicles (ER–horse, siGRP94–RBCVs, and siGRP94–CCVs) marked by siGRP94–FITC into HepG2 cells during 0–1 h. **i** Interaction of STIM1 (red, marked by anti–STIM1) and ORAI1 (yellow, marked by anti–ORAI1). The co–localization rate was calculated by Pearson's correlation analysis to be 84.48 ± 3.16%. The data are expressed as the mean ± SD (n = 3); a single asterisk indicates $p < 0.05$, double asterisks indicate $p < 0.01$ and triple asterisks indicate $p < 0.001$.

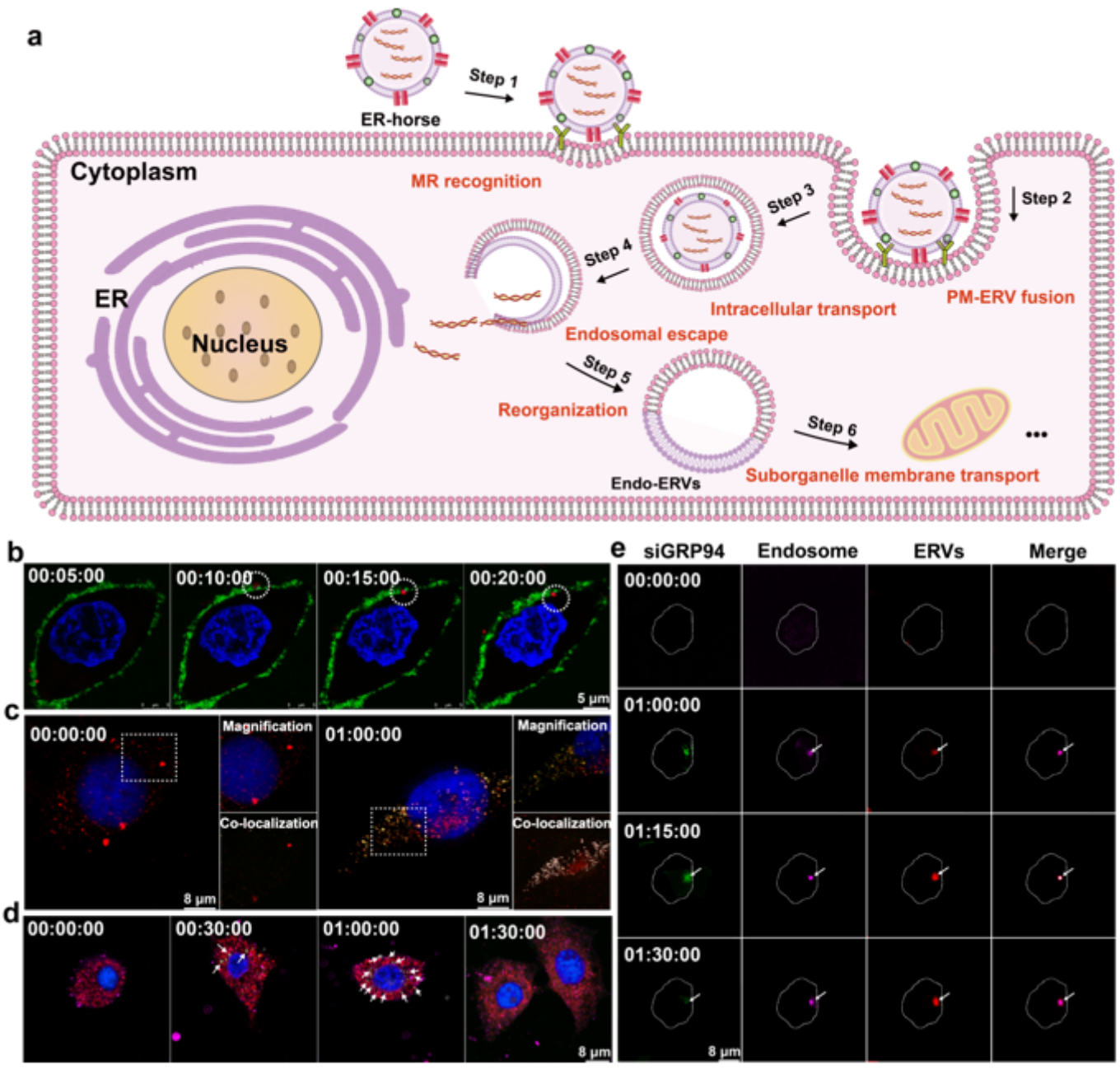

Figure 4

Intracellular tracing of the ER–horse and cytosolic delivery mechanism. a Schematic illustration of the intracellular trafficking pathways of ER–horse. **b** ER–horse fusion with the HepG2 PM was monitored by live–cell imaging. The PM is labeled with DiO (green). ER–horse is labeled with CNX antibody (red). Cell nuclei were stained with DAPI (blue). Scale bar = 5 μm. **c** Confocal images of HepG2 cells incubated with ER–horse showing the relative localization of the dextran–FITC–labeled endosomes (green) and the ER–horse (red, marked by DiO) at incubation times of 0 min and 60 min. Scale bar = 8 μm. Magnified confocal microscopy images of the regions are shown at the top right corner of each group. Scale bar = 5 μm. Co–localization images of magnified endosomes and ER–horse are shown at the bottom right corner of each group. Scale bar = 8 μm. **d** siGRP94 from Endo–ERVs released in ER. Confocal images of HepG2 cells incubated with siGRP94–loaded ER–horse showing the localization of the endosomes (labeled with EEA1 antibody, purple) siGRP94 (green, marked by FITC) and ER (labeled with CNX antibody, red) at incubation times of 30, 60 and 90 min. **e** Intracellular tracing of siGRP94 molecules, endosomes and ER–horse. HepG2 cells were incubated with ER–horse, and the interaction was monitored by live–cell imaging at 0, 60, 75 and 90 min. The endosomes are labeled with Alexa 647–dextran (purple). siGRP94 molecules are labeled with FITC (green). ERVs are labeled with DiO (red). Scale bar = 8 μm.

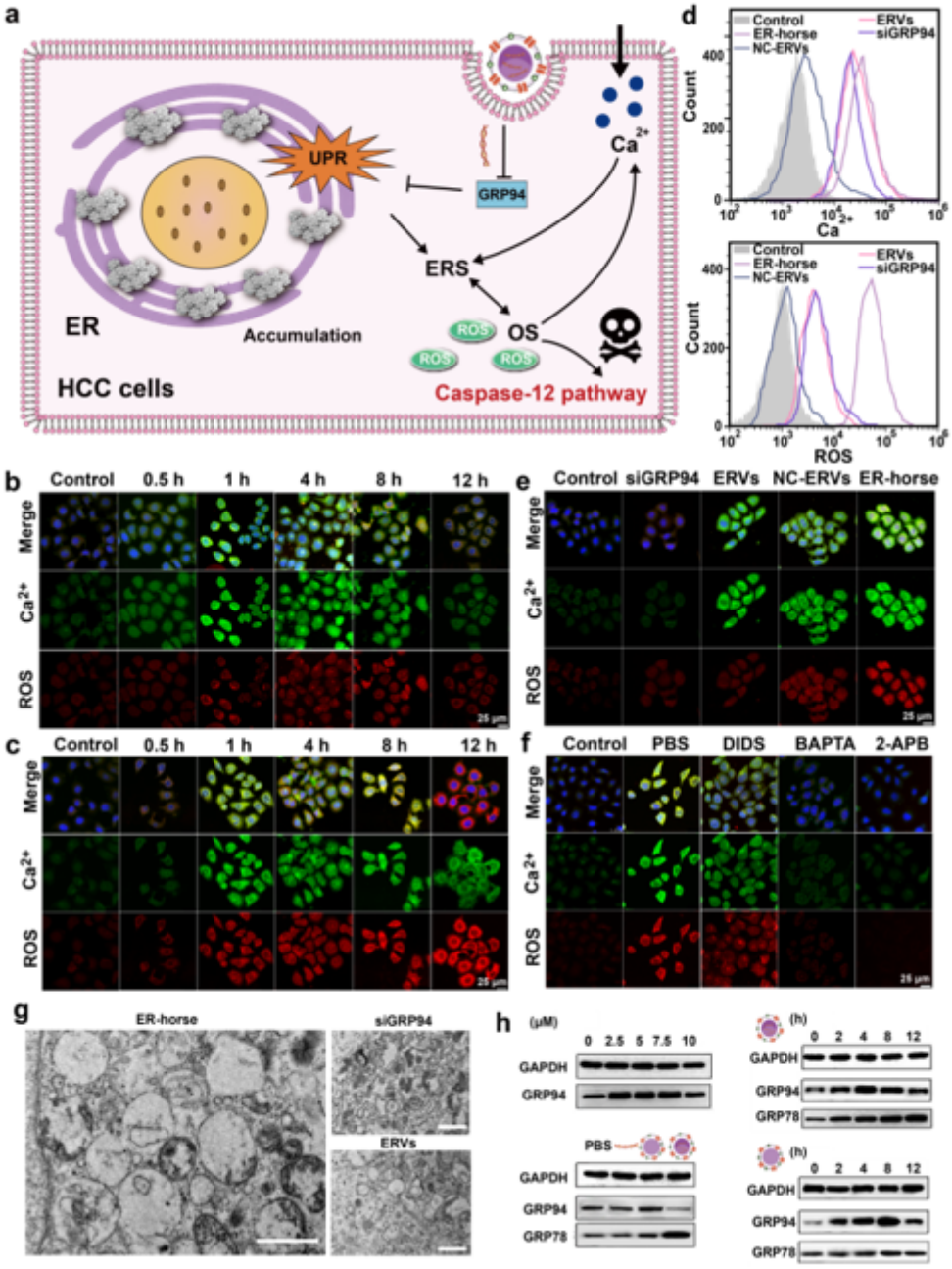

Figure 5

Mechanism of intracellular Ca^{2+} ($[Ca^{2+}]i$) accumulation (green, marked by Fluo–4AM) and ROS overproduction (red, marked by dihydroethidium (DHE)). a Schematic illustration of the Ca^{2+} homeostasis disruption–inducing effect triggered by ERVs and ER–horse. **b** Determination of the intracellular Ca^{2+} concentration and the production of ROS in HepG2 cells after incubation with ERVs for 0, 0.5, 1, 4, 8 and 12 h. **c** Determination of the intracellular Ca^{2+} concentration and the production of ROS in HepG2 cells after incubation with ER–horse for 0, 0.5, 1, 4, 8 and 12 h. **d** Determination of the intracellular Ca^{2+} concentration (top) and the production of ROS (bottom) in HepG2 cells after different treatments for 1 h (PBS, free–siGRP94, ERVs, NC–ERVs, ER–horse) as monitored by flow cytometry. **e** Determination of the intracellular Ca^{2+} concentration and the production of ROS in HepG2 cells incubated with different

treatments for 1 h (PBS, free–siGRP94, ERVs, NC–ERVs, ER–horse). **f** Determination of the intracellular Ca^{2+} concentration and the production of ROS in HepG2 cells incubated with ER–horse after pretreatment with different drugs that affect Ca^{2+} concentrations (the voltage–dependent anion channel type 1 calcium channel inhibitor DIDS, the calcium chelator BAPTA, and the ORAI1 inhibitor 2–APB). **g** HepG2 cells were exposed to ER–horse, ERVs, and siGRP94 for 0 h and 36 h, and then the ultrastructure of the ER was detected by TEM. The scale bar indicates 1 μm. **h** Expression of ERS–related proteins under the above treatments in the HepG2 cells. The upper left image showe the gene–silencing effects of different concentrations of ER–horse (0, 2.5, 5, 7.5 and 10 μM, quantified by siGRP94) after 24 h of incubation. The bottom left image shows the effectiveness of different treatments (PBS, siGRP94, ERVs, ER–horse) in inducing ERS and apoptosis after 36 h of incubation. The right image shows the effectiveness of ER–horse and ERVs in inducing ERS and inhibiting the UPR after incubation for different times (0, 2, 4, 8 and 12 h). GRP94 and GRP78 are both marker proteins of ERS and the UPR.

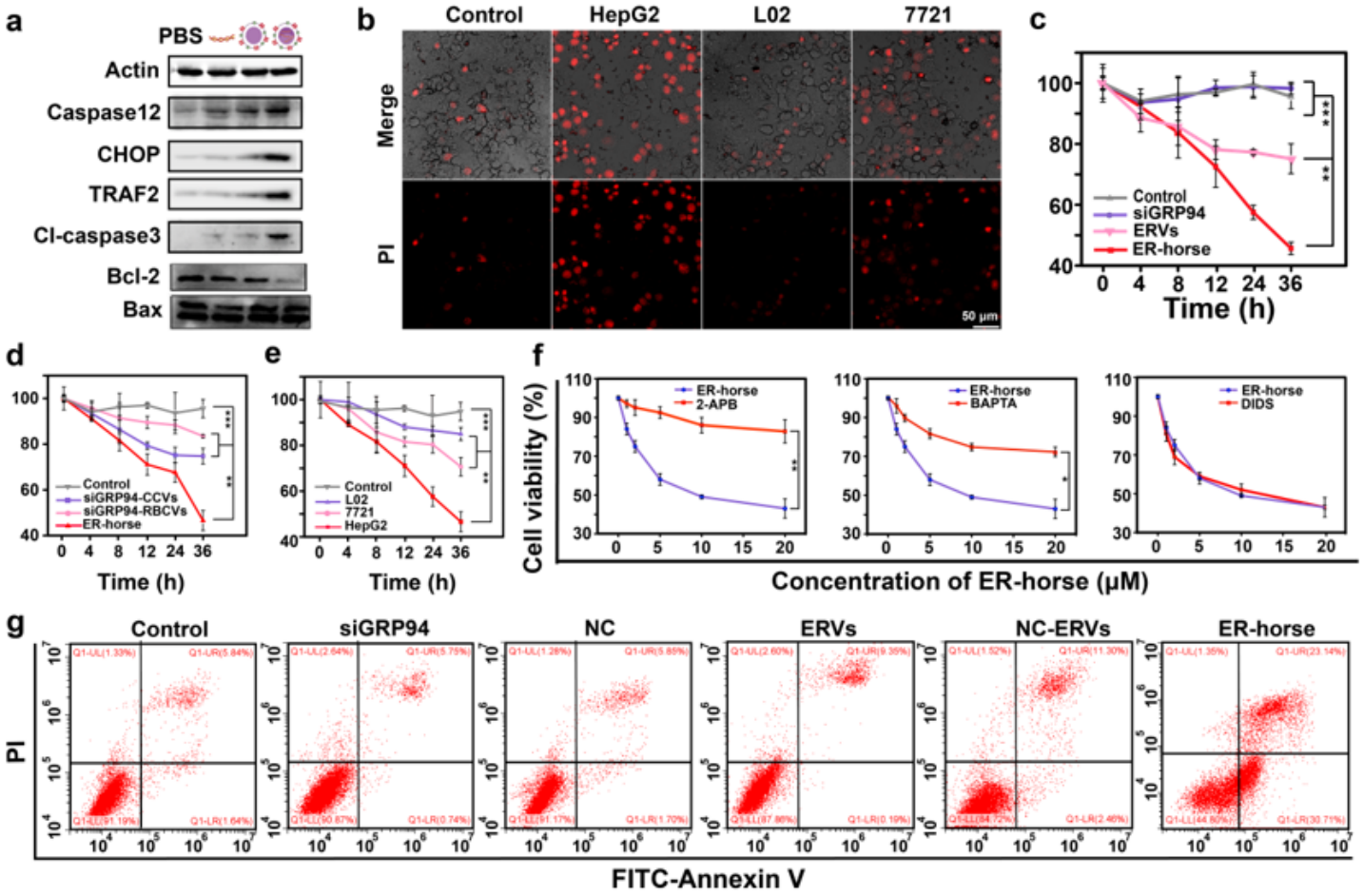

Figure 6

In vitro therapeutic efficacy of ER–horse. a Expression of apoptosis–related proteins under the above treatments in the HepG2 cells. **b** CLSM images showing the cell survival analysis of HepG2 cells, L02 cells and 7721 cells upon treatment with ER–horse. The apoptotic cells were stained with PI dye. **c** CCK–

8 assay results showing the cell proliferation/viability of HepG2 cells after incubation with different treatments (PBS, free–siGRP94, ERVs, ER–horse). **d** CCK–8 assay results showing cell proliferation/viability of HepG2 cells after incubation with different vesicles (ER–horse, siGRP94–RBCVs, siGRP94–CCVs). **e** CCK–8 assay results showing cell proliferation/viability of HepG2 cell, L02 cell and 7721 cell upon treatment with ER–horse. **f** CCK–8 assay results showing the viability of HepG2 cell proliferation after incubation with ER–horse after pretreatment with different drugs (2–APB, BAPTA, DIDS). **g** Flow cytometry analysis showing the apoptosis of HepG2 cells upon the different treatments (PBS, siGRP94, NC, ERVs, NC–ERVs, ER–horse). The data are expressed as the mean ± SD (n = 3); a single asterisk indicates $p < 0.05$, double asterisks indicate $p < 0.01$ and triple asterisks indicate $p < 0.001$.

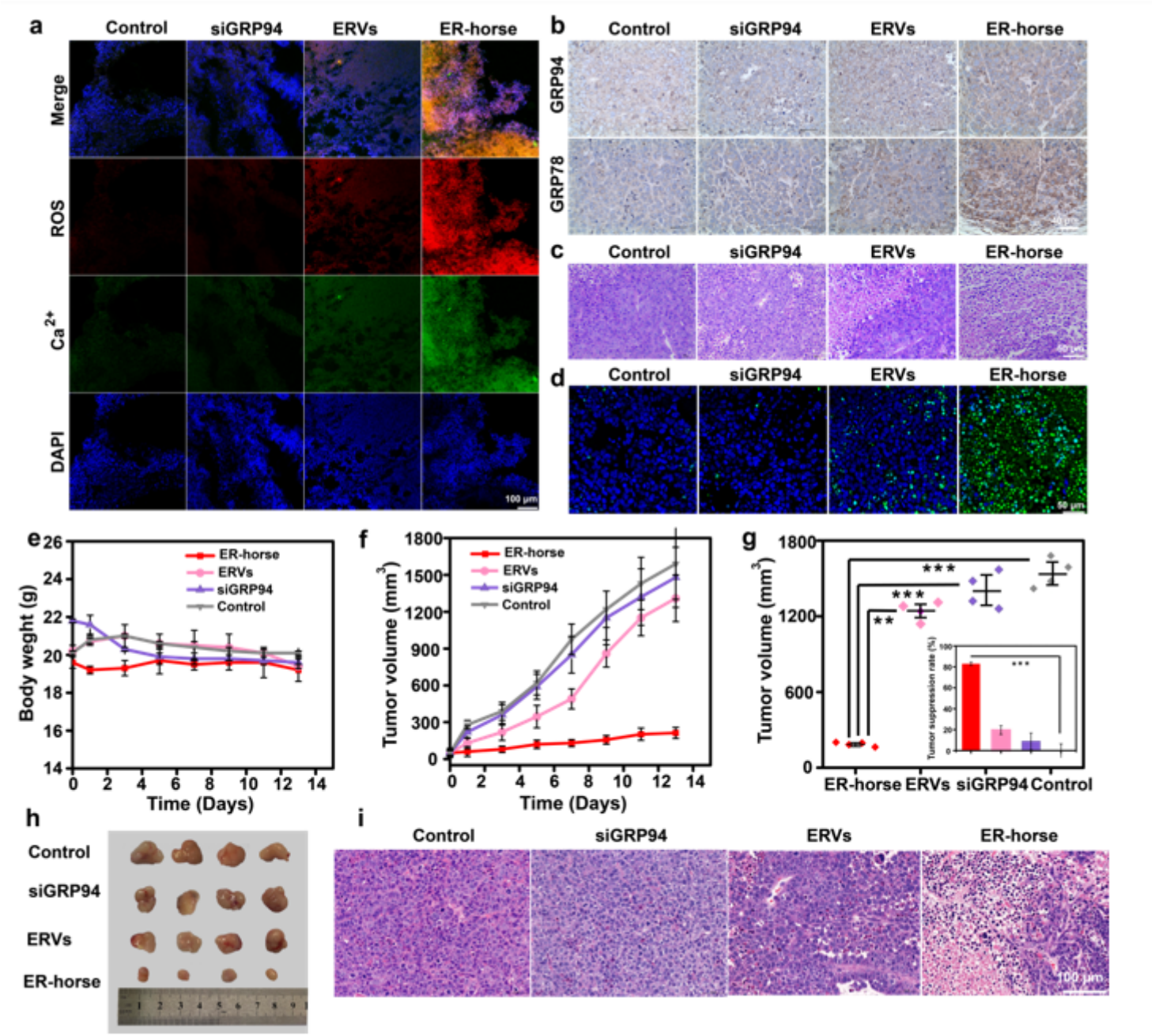

Figure 7

Therapeutic efficacy of ER–horse in vivo. a Determination of the intracellular Ca^{2+} concentration (green, marked by Fluo–4AM) and the production of ROS (red, marked by DHE) in tumors injected with different treatments (PBS, siGRP94, ERVs, ER–horse). Scale bar = 100 μm. **b** IHC of ERS–related protein expression (GRP94 and GRP78) under different treatment conditions (PBS, siGRP94, ERVs, ER–horse) in tumor tissues after 36 h of treatment. Scale bar = 40 μm. **c** Representative H&E–stained histological sections of tumor tissues after the same treatments as **a**. Scale bar = 50 μm. **d** TUNEL staining of histological sections of tumor tissues after the same treatments as a). Scale bar = 50 μm. **e** The body weight of the mice with different treatments of via tail vein injected (PBS, siGRP94, ERVs, ER–horse) every other day. The data are expressed as the mean ± SD (n = 4). **f** Tumor volume curves of mice during the same treatments as a). The data are expressed as the mean ± SD (n = 4). **g** Tumor volumes at day 15 (sacrifice two days after the treatment) after the same treatments as **a**. The data are expressed as the mean ± SD (n = 4). The lower right frame indicates the percentage of tumor growth inhibition of different groups compared to control group. **h** Representative photographs showing the appearance of tumor–bearing nude mice and the tumors at the end of treatment. **i** Representative H&E stains histological sections of tumor tissues after the same treatments as **e**. Scale bar = 100 μm.

Supplementary Files

This is a list of supplementary files associated with this preprint. Click to download.

- SupportingInformation.docx